RSC Advances

PAPER

View Article Online
View Journal | View Issue

Cite this: *RSC Adv.*, 2019, **9**, 42470

Intrinsic poorly-crystallized $Fe_5O_7(OH)\cdot 4H_2O$: a highly efficient oxygen evolution reaction electrocatalyst under alkaline conditions†

Xiaoteng Ding,‡[a] Wei Cui,‡[b] Xiaohua Zhu,[c] Jianwei Zhang*[d] and Yusheng Niu *[a]

Received 15th August 2019
Accepted 4th December 2019

DOI: 10.1039/c9ra06374a

rsc.li/rsc-advances

As the bottleneck of electrochemical overall water splitting, the oxygen evolution reaction (OER) needs efficient catalysts to lower the required overpotential. Electrocatalysts with an amorphous form are highly active but suffer with low structural stability. Poorly crystallized materials with activity like amorphous forms, while maintaining the mechanical robustness of crystalline forms, are expected to be ideal materials. Towards this direction, we, for the first time, developed low-crystalline $Fe_5O_7(OH)\cdot 4H_2O$ as an excellent OER electrocatalyst with an overpotential of 269 mV, in order to drive a current density of 100 mA cm^{-2} in a 1.0 M KOH environment, and this outperforms most of the reported Fe-based electrocatalysts. Notably, its activity can be maintained for at least 100 hours. A one-pot synthesis for the poorly-crystallized material using one of the most abundant metal elements to obtain effective OER catalysis will provide great convenience in practical applications.

Introduction

The ever-increasing depletion of fossil fuels and worsening environmental contamination stimulate extensive research into clean and efficient energy generation systems.[1–3] Among these, electrochemical water splitting has attracted significant attention due to hydrogen production utilizing electricity from renewable but intermittent sources such as solar energy, wind, wave power, *etc.*[4,5] However, the associated energy conversion efficiency is greatly limited by the sluggish oxygen evolution reaction (OER), which is a complex four-electron redox process.[6–9] IrO_2 and RuO_2, as the most efficient electrocatalysts, exhibit high OER activity, yet their low-abundance and high cost dramatically hinder commercial utilization.[10] Alternatives based on earth-abundant and inexpensive transition-metal based materials are actively being pursued.

As non-precious-metal compounds, Fe-based oxides can serve as active OER electrocatalysts, but they are restricted by their low conductivity and chemical stability.[11–16] Highly crystallized Fe nitrides,[17–20] phosphides,[21–23] sulfides,[24] *etc.* have better electronic conductive properties and are more thermodynamically/chemically stable, exhibiting progressive OER activity. However, their electrocatalytic performances are still far from the requirements of practical applications. A challenging route, the topological transformation strategy towards an amorphous structure, has been developed to improve OER dynamics by increasing the intrinsic activity and exposing more active sites. However, the resulting non-crystallized materials are generally susceptible to unavoidable collapse to some degree, exhibiting unsatisfactory robustness.[25–27] Designing poorly-crystallized materials with excellent catalytic activity similar to the amorphous form, and with structural stabilization of crystallization will provide a fresh and efficient perspective towards an ideal model.

On the basis of the above consideration, low-crystalline $Fe_5O_7(OH)\cdot 4H_2O$ was proposed and was developed by a one-pot hydrothermal method in the presence of Ni foam (NF). Such material anchoring on NF ($Fe_5O_7(OH)\cdot 4H_2O$/NF) demonstrates excellent OER activity with an overpotential of 269 mV to drive 100 mA cm^{-2} current density in a 1.0 M KOH environment, outperforming most of the reported Fe-based electrocatalysts. More remarkably, its activity can be maintained for at least 100 h. It is shown that the highly efficient electrocatalytic OER performance lies in the unrivaled structure superiority, stemming from the poor-crystallization state that is caused by the existence of massive oxygen-deficiencies.

Results and discussion

Fig. 1a shows the X-ray diffraction (XRD) pattern of the solvothermally obtained products. The diffraction peaks at 36.08°, 40.54°, 46.43°, 53.15°, 61.32°, and 63.02° are indexed to the

[a]*School of Tourism and Geography Sciences, College of Life Sciences, Qingdao University, Qingdao 266071, China. E-mail: nys@qdu.edu.cn*

[b]*Human Resources Department, Qingdao University, Qingdao 266071, China*

[c]*Key Laboratory of Eco-geochemistry, Ministry of Natural Resources, National Research Center for Geoanalysis, Beijing 100037, China*

[d]*School of Environmental Science and Engineering, Qingdao University, Qingdao 266071, China. E-mail: sdqdzjw@qdu.edu.cn*

† Electronic supplementary information (ESI) available. See DOI: 10.1039/c9ra06374a

‡ Xiaoteng Ding and Wei Cui contributed equally to this work.

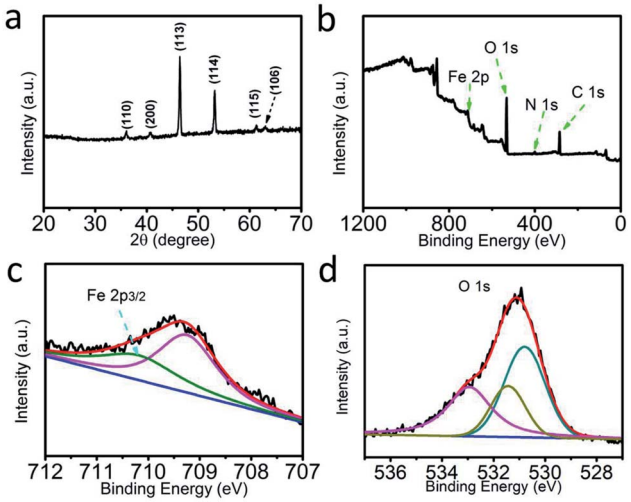

Fig. 1 (a) XRD pattern of $Fe_5O_7(OH)\cdot 4H_2O$. (b) XPS survey spectrum of $Fe_5O_7(OH)\cdot 4H_2O$. XPS spectra of $Fe_5O_7(OH)\cdot 4H_2O$ in the (c) Fe 2p and (d) O 1s regions.

(110), (200), (113), (114), (115), and (106) crystal planes of $Fe_5O_7(OH)\cdot 4H_2O$, respectively (JCPDS No. 29-0712).[28] Moreover, X-ray photoelectron spectroscopy (XPS) characterization was performed on the resulting $Fe_5O_7(OH)\cdot 4H_2O$. The corresponding XPS survey spectrum (Fig. 1b) provides evidence for the presence of Fe and O elements. The N element should be derived from the adsorbed ferric nitrate impurity.[29] In the Fe 2p region (Fig. 1c), the binding energy (BE) of 709.2 eV can be attributed to the ferric nitrate adsorbed on the $Fe_5O_7(OH)\cdot 4H_2O$ nanocrystallites. The peak at 710.2 eV is assigned to the BE of Fe $2p_{3/2}$ in $Fe_5O_7(OH)\cdot 4H_2O$.[29] Moreover, the peaks centered at 530.4 eV, 531.2 eV, and 533.1 eV in the O 1s region (Fig. 1d) are ascribed to the Fe–O bond, the oxygen vacancies and the hydroxyl group, respectively, in the $Fe_5O_7(OH)\cdot 4H_2O$.

Fig. 2a and b show the scanning electron microscopy (SEM) images of $Fe_5O_7(OH)\cdot 4H_2O$/NF. It can be seen that the $Fe_5O_7(OH)\cdot 4H_2O$ nanosheets grow tightly on the NF and form arrays on the NF. The Brunauer–Emmett–Teller (BET) tests revealed that the surface area of $Fe_5O_7(OH)\cdot 4H_2O$/NF is 50.2 cm^2. The associating transmission electron microscopy (TEM) image of $Fe_5O_7(OH)\cdot 4H_2O$ further confirms its nanosheet structure (Fig. 2c), and the high-resolution TEM (HRTEM) image demonstrates that the lattice is not well-defined (Fig. 2d), due to its intrinsic poorly-crystallized state. The electron spin resonance (ESR) spectroscopy determination unveils the presence of a surface oxygen vacancy. The obtained samples show two distinct symmetrical ESR signal peaks at $g = 2.002$ (Fig. S1†). The corresponding selected area electron diffraction (SAED) pattern shows rings indexed to the (115) and (110) planes of $Fe_5O_7(OH)\cdot 4H_2O$. Energy-dispersive X-ray (EDX) elemental mapping images of $Fe_5O_7(OH)\cdot 4H_2O$/NF (Fig. 2e and f) also show that Fe and O elements are uniformly distributed in the $Fe_5O_7(OH)\cdot 4H_2O$ product.

The electrochemical OER performance was examined in 1.0 M KOH using a typical three-electrode configuration.

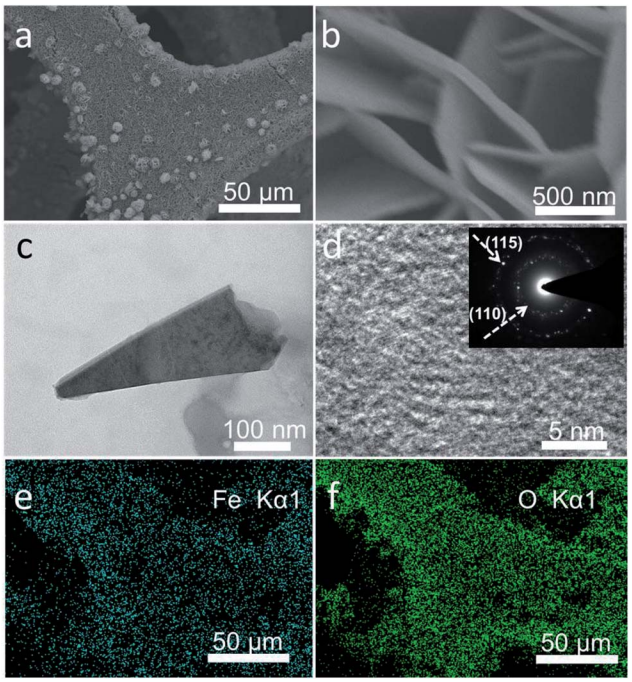

Fig. 2 (a and b) SEM images for $Fe_5O_7(OH)\cdot 4H_2O$/NF. (c) TEM image of one single $Fe_5O_7(OH)\cdot 4H_2O$ nanosheet. (d) HRTEM image and SADE pattern for the $Fe_5O_7(OH)\cdot 4H_2O$ nanosheet. EDX elemental mapping images of (e) Fe and (f) O.

$Fe_5O_7(OH)\cdot 4H_2O$/NF ($Fe_5O_7(OH)\cdot 4H_2O$ loading: 0.6 mg cm^{-2}) was used as the working electrode, while Hg/HgO (filled with 6 M KOH solution) and a graphite plate were utilized as the reference and counter electrodes, respectively. For comparison, NF and RuO_2 deposited on NF (RuO_2/NF, RuO_2 loading: 0.6 mg cm^{-2}) were also tested under the same conditions. Considering ohmic potential drop (iR) losses, experimental data were all

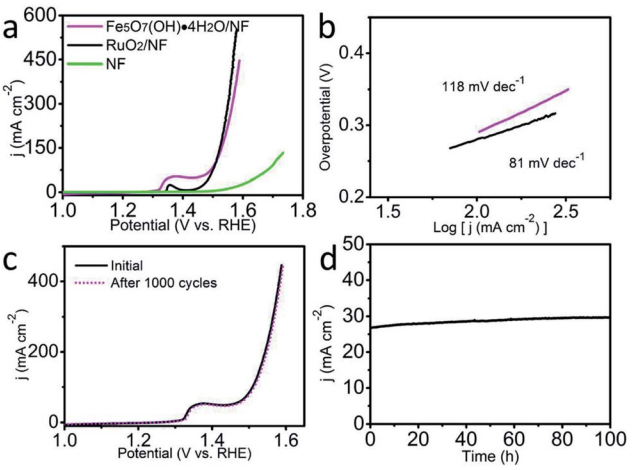

Fig. 3 (a) LSV curves of $Fe_5O_7(OH)\cdot 4H_2O$/NF, RuO_2/NF and bare NF for OER. (b) Corresponding Tafel plots for $Fe_5O_7(OH)\cdot 4H_2O$/NF and RuO_2/NF. (c) LSV curves for $Fe_5O_7(OH)\cdot 4H_2O$/NF before and after 1000 CV cycles. (d) Time-dependent current density curve of $Fe_5O_7(OH)\cdot 4H_2O$/NF. All experiments were tested in 1.0 M KOH.

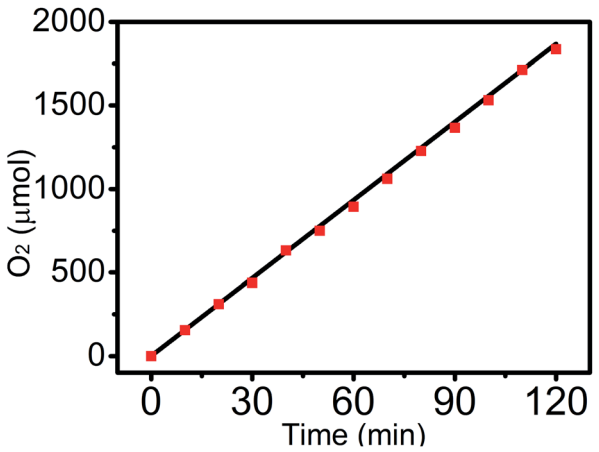

Fig. 4 The amount of oxygen theoretically calculated and experimentally measured *versus* time for $Fe_5O_7(OH)\cdot 4H_2O$/NF in 1.0 M KOH.

corrected for further analysis, thus directly reflecting the intrinsic behavior of the catalysts. The overpotentials were converted and reported as values *vs.* the reversible hydrogen electrode (RHE). As observed from the linear sweep voltammetry (LSV) curves in Fig. 3a, $Fe_5O_7(OH)\cdot 4H_2O$/NF demonstrates an outstanding catalytic activity with an overpotential of 269 mV to drive 100 mA cm^{-2} in 1.0 M KOH, outperforming most of the reported Fe-based electrocatalysts such as Ni–Fe LDH (269 mV – 5 mA cm^{-2}),[30] Ni–Fe LDH/CNT (269 mV – 40 mA cm^{-2}),[31] FeOOH/Au (450 mV – 9 mA cm^{-2}),[32] *etc.* (Table S1†). More impressively, such an electrocatalytic performance even surpasses that of RuO_2/NF (279 mV, 100 mA cm^{-2}). As for the Tafel plots shown in Fig. 3b, RuO_2/NF gives a Tafel slope of 81 mV dec^{-1}. The corresponding Tafel slope for $Fe_5O_7(OH)\cdot 4H_2O$/NF (118 mV dec^{-1}) is relatively larger than that for RuO_2/NF, implying the further engineering requirement towards more favorable catalytic kinetics. The high surface area of the array structure, affirmed by the BET measurements, and the existence of abundant oxygen-defects verified by the electron spin resonance spectrum, both contribute to the outstanding catalytic activity. The intrinsic oxygen-defects of $Fe_5O_7(OH)\cdot 4H_2O$ result in its poorly-crystallized state. We deliberately treated the sample under high-temperature and the degraded catalytic activity was observed, related to the overpotentials of 280 mV and 480 mV to deliver 15 mA cm^{-2} and 100 mA cm^{-2}, respectively (Fig. S2†). However, such a performance of the sample after high-temperature treatment is still very attractive for scientific researchers. To further gain insight into the excellent OER activity of $Fe_5O_7(OH)\cdot 4H_2O$, we examined the electrochemical double layer capacitances (C_{dl}), proportional to the electrochemical surface area (ECSA), for $Fe_5O_7(OH)\cdot 4H_2O$/NF. Fig. S3† presents the corresponding cyclic voltammograms. The slope for the linear plot of the non-faradaic capacitance currents as a function of scan rates is the value of C_{dl}. The C_{dl} for $Fe_5O_7(OH)\cdot 4H_2O$/NF is 18 mF cm^{-2}, and ECSA was determined to be 45 cm^2 on the basis of the equation: ECSA = C_{dl}/0.4. A series of cyclic voltammograms for $Fe_5O_7(OH)\cdot 4H_2O$/NF and $Fe_5O_7(OH)\cdot 4H_2O$/NF after heat treatment were collected, and are shown in Fig. S4.† A linear plot related to the oxidation currents for the redox species as a function of the scan rates can be obtained from the cyclic voltammograms, and the turnover frequency (TOF) was determined to be 0.017 mol of O_2 s^{-1} at an overpotential of 269 mV for $Fe_5O_7(OH)\cdot 4H_2O$/NF, and this is superior to those of samples after heat treatment (0.00468 mol O_2 s^{-1} for overpotential of 300 mV). The long-term stability of $Fe_5O_7(OH)\cdot 4H_2O$/NF was also evaluated by continuous cyclic voltammetry scanning at a scan rate of 100 mV s^{-1}. After 1000 cycles in 1.0 M KOH, the obtained LSV curve almost coincides with the initial one (Fig. 3c). The superb durability of $Fe_5O_7(OH)\cdot 4H_2O$/NF was also recorded by OER electrolysis at a fixed overpotential, preserving its catalytic activity for at least 100 h (Fig. 3d).

The experimentally emerging gas species was qualitatively determined by gas chromatography analysis and was further qualified using a calibrated pressure sensor, monitoring the pressure change in the anodic compartment of the H-type electrolytic cell. The faradaic efficiency (FE) of $Fe_5O_7(OH)\cdot 4H_2O$/NF was then calculated to be 100% by comparing the molar number of the practically evolved oxygen with the theoretically calculated number (Fig. 4).

Conclusions

In summary, poorly-crystallized $Fe_5O_7(OH)\cdot 4H_2O$ was designed and exploited by a one-pot hydrothermal method as a high-efficiency water-oxidation electrocatalyst. Profiting from its low-crystallization state, such a material exhibits a low overpotential of 269 mV at 100 mA cm^{-2} current density, exceeding most of the reported Fe-based electrocatalysts. More encouragingly, the activity can be maintained for at least 100 h. This current work not only provides an outstanding OER electrocatalyst, but also demonstrates a new avenue to construct highly efficient poorly-crystallized catalysts, by a relatively quick method using one of the most abundant metal elements, for other electrocatalytic systems.

Conflicts of interest

There are no conflicts to declare.

Acknowledgements

This work was supported by the National Natural Science Foundation of China (No. 21575137).

References

1 T. R. Cook, D. K. Dogutan, S. Y. Reece, Y. Surendranath, T. S. Teets and D. G. Nocera, *Chem. Rev.*, 2010, **110**, 6474–6502.
2 S. Chu and A. Majumdar, *Nature*, 2012, **488**, 294–303.
3 S. Chu, Y. Cui and N. Liu, *Nat. Mater.*, 2016, **16**, 16–22.
4 F. Song, L. Bai, A. Moysiadou, S. Lee, C. Hu, L. Liardet and X. Hu, *J. Am. Chem. Soc.*, 2018, **140**, 7748–7759.

5 D. Chen, M. Qiao, Y. R. Lu, L. Hao, D. Liu, C.-L. Dong, Y. Li and S. Wang, *Angew. Chem., Int. Ed.*, 2018, **57**, 8691–8696.
6 M. Goerlin, J. Ferreira de Araújo, H. Schmies, D. Bernsmeier, S. Dresp, M. Gliech, Z. Jusys, P. Chernev, R. Kraehnert, H. Dau and P. Strasser, *J. Am. Chem. Soc.*, 2017, **139**, 2070–2082.
7 M. Tahir, L. Pan, F. Idrees, X. Zhang, L. Wang, J. Zou and Z. Wang, *Nano Energy*, 2017, **37**, 136–157.
8 B. M. Hunter, H. B. Gray and A. M. Muller, *Chem. Rev.*, 2016, **116**, 14120–14136.
9 N. T. Suen, S. F. Hung, Q. Quan, N. Zhang, Y. Xu and H. Chen, *Chem. Soc. Rev.*, 2017, **46**, 337–365.
10 F. Dionigi and P. Strasser, *Adv. Energy Mater.*, 2016, **6**, 1600621.
11 L. Han, S. Dong and E. Wang, *Adv. Mater.*, 2016, **28**, 9266–9291.
12 A. Indra, P. W. Menezes, N. R. Sahraie, A. Bergmann, C. Das, M. Tallarida, D. Schmeiber, P. Strasser and M. Driess, *J. Am. Chem. Soc.*, 2014, **136**, 17530–17536.
13 H. Yang, Y. Liu, S. Luo, Z. Zhao, X. Wang, Y. Luo, Z. Wang, J. Jin and J. Ma, *ACS Catal.*, 2017, **7**, 5557–5567.
14 T. Li, Y. Lv, J. Su, Y. Wang, Q. Yang, Y. Zhang, J. Zhou, L. Xu, D. Sun and Y. Tang, *Adv. Sci.*, 2017, **4**, 1700226.
15 X.-F. Lu, L.-F. Gu, J.-W. Wang, J.-X. Wu, P.-Q. Liao and G.-R. Li, *Adv. Mater.*, 2017, **29**, 1604437.
16 B. K. Kang, M. H. Woo, J. Lee, Y. H. Song, Z. Wang, Y. Guo, Y. Yamauchi, J. H. Kim, B. Lim and D. H. Yoon, *J. Mater. Chem. A*, 2017, **5**, 4320–4324.
17 F. Yu, H. Zhou, Z. Zhu, J. Sun, R. He, J. Bao, S. Chen and Z. Ren, *ACS Catal.*, 2017, **7**, 2052–2057.
18 B. Zhang, C. Xiao, S. Xie, J. Liang, X. Chen and Y. Tang, *Chem. Mater.*, 2016, **28**, 6934–6941.
19 Y. Fan, S. Ida, A. Staykov, T. Akbay, H. Hagiwara, J. Matsuda, K. Kaneko and T. Ishihara, *Small*, 2017, **13**, 1700099.
20 Y. Zhang, K. Rui, Z. Ma, W. Sun, Q. Wang, P. Wu, Q. Zhang, D. Li, M. Du, W. Zhang, H. Lin and J. Zhu, *Chem. Mater.*, 2018, **30**, 4762–4769.
21 D. Li, H. Baydoun, B. Kulikowski and S. L. Brock, *Chem. Mater.*, 2017, **29**, 3048–3054.
22 J. Xu, J. Li, D. Xiong, B. Zhang, Y. Liu, K.-H. Wu, I. Amorim, W. Li and L. Liu, *Chem. Sci.*, 2018, **9**, 3470–3476.
23 Y. Tian, H. Wang, P. Liu, Y. Shen, C. Cheng, A. Hirata, T. Fujita, Z. Tang and M. Chen, *Energy Environ. Sci.*, 2016, **9**, 2257–2261.
24 X. Zou, Y. Wu, Y. Liu, D. Liu, W. Li, L. Gu, H. Liu, P. Wang, L. Sun and Y. Zhang, *Chem*, 2018, **4**, 1139–1152.
25 L. Xie, R. Zhang, L. Cui, D. Liu, S. Hao, Y. Ma, G. Du, A. M. Asiri and X. Sun, *Angew. Chem., Int. Ed.*, 2017, **56**, 1064–1068.
26 M. Ma, F. Qu, X. Ji, D. Liu, S. Hao, G. Du, A. M. Asiri, Y. Yao, L. Chen and X. Sun, *Small*, 2017, **13**, 1700394.
27 K. Xu, H. Cheng, L. Liu, H. Lv, X. Wu, C. Wu and Y. Xie, *Nano Lett.*, 2017, **17**, 578–583.
28 X. Gong, J. Li, Y. Lin, X. Liu, L. Chen, J. Li and D. Li, *Chin. Sci. Bull.*, 2014, **59**, 3904–3911.
29 L. Lin, J. Li, Y. Lin, X. Liu, L. Chen, J. Fu and D. Li, *Mater. Res. Innovations*, 2015, **19**, 118–124.
30 D. Tang, J. Liu, X. Wu, R. Liu, X. Han, Y. Han, H. Huang, Y. Liu and Z. Kang, *ACS Appl. Mater. Interfaces*, 2014, **6**, 7918–7926.
31 M. Gong, Y. Li, H. Wang, Y. Liang, J. Z. Wu, J. Zhou, J. Wang, T. Regier, F. Wei and H. Dai, *J. Am. Chem. Soc.*, 2013, **135**, 8452–8455.
32 S. Zou, M. S. Burke, M. G. Kast, J. Fan, N. Danilovic and S. W. Boettcher, *Chem. Mater.*, 2015, **27**, 8011–8020.